J Adv Ceram

Research Article

Dual-sensitized Gd-based oxyfluoride glass with enhanced scintillation for superior X-ray imaging

Dandan Zhang[1], Shisheng Lin[2,✉], Yinsheng Xu[1,✉], Jing Ren[3], Weiwei Li[4], Xianghua Zhang[1,5], Daqin Chen[2,✉]

Cite this article: Zhang D, Lin S, Xu Y, et al. *J Adv Ceram* 2026, **15**(3): 9221259. https://doi.org/10.26599/JAC.2026.9221259

ABSTRACT: Rare-earth-doped glasses have been demonstrated as highly promising scintillator materials, particularly for X-ray imaging applications. However, challenges such as high defect density, low luminescence efficiency, and poor spatial resolution remain, primarily attributed to high phonon energy, inefficient energy transfer (ET), and light scattering in glass materials. Herein, we report a successfully designed dual-sensitized codoped Gd-based oxyfluoride glass scintillator that can achieve high internal quantum efficiency (IQE, 97.5%), excellent X-ray luminescence (XEL) intensity (216% $Bi_4Ge_3O_{12}$), high optical transparency (approximately 90% at 550 nm), and good radiation stability by using Tb^{3+} as the luminescent center, synergistically incorporating Gd^{3+} and Ce^{3+}. Specifically, the optimized glass scintillator can achieve a spatial resolution of up to 32.6 lp·mm^{-1} for X-ray imaging, coupled with an exceptionally low detection limit of 1.03 μGy·s^{-1}. Additionally, the developed glass scintillator enables irregular-shaped and large-scale fabrication (diameter: 5 cm) that is difficult to accomplish with conventional scintillator materials. The developed material offers a new option for developing low-cost, high-performance glass scintillators for high-resolution X-ray imaging.

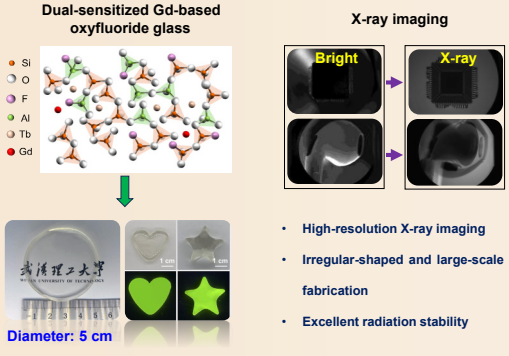

KEYWORDS: glass scintillators; rare earth; energy transfer (ET) mechanism; X-ray imaging

1 Introduction

X-ray imaging plays an increasingly critical role in a variety of fields, including medical diagnostics, security screening, and industrial nondestructive testing [1]. However, the current X-ray imaging technology encounters challenges such as low spatial resolution, low X-ray energy utilization, and poor large-area uniformity, which impose strict limitations on the further development of this technology [2,3]. In fact, as the core component of X-ray imaging systems, the exploration of highly efficient scintillating materials is crucial for enhancing the imaging performance. However, although traditional single-crystal scintillators (e.g., NaI:Tl [4], $Bi_4Ge_3O_{12}$ [5], and $Lu_3Al_5O_{12}$:Ce [6]) offer the advantage of high light yield (LY), their application in large-area imaging is restricted by the high cost and formidable technical challenges involved in fabricating large-area, high-quality crystals [7,8].

In contrast, glass scintillators have emerged as a cost-effective and versatile alternative to traditional single crystals due to their tunable composition, high transparency, and manufacturing scalability, and even optical fiber form, to meet different device requirements [6,9–12]. Rare earth ions (e.g., Ce^{3+}, Tb^{3+}, and Eu^{3+}) as luminescent centers in glass scintillators are a simple, efficient, and attractive strategy [13–20]. In particular, Tb^{3+} is suitable for X-ray imaging and neutron detection techniques because the position of its emission peak (544 nm) matches the detection range of charge-coupled devices (CCDs) [21–24]. For glass scintillators, the option of the amorphous structure plays an essential role in scintillation performance; among them, the lithium aluminosilicate (LAS) oxyfluoride glass system, known for its lower phonon energy and chemical stability, is chosen as the main subject for research on glass scintillators [25,26]. On the one hand, the LAS oxyfluoride glass can exhibit high solubility (up to 10 wt%) of Tb^{3+} ions, primarily attributed to Li^+ doping increasing the number of nonbridging oxygen atoms, which significantly enhances the uniformity of Tb^{3+} distribution within the glass matrix [27]. On the other hand, the 4f–5d energy level leap of Tb^{3+} needs the phonon energy of the LAS glass host to be less than its energy level difference (~3500 cm^{-1}), and the corresponding nonradiative leap can be effectively suppressed by introducing

[1] State Key Laboratory of Silicate Materials for Architectures, Wuhan University of Technology, Wuhan 430070, China. [2] College of Physics and Energy, Fujian Provincial Key Laboratory of Quantum Manipulation and New Energy Materials, Fujian Normal University, Fuzhou 350117, China. [3] Key Laboratory of In-Fiber Integrated Optics of Ministry of Education, College of Physics and Optoelectronic Engineering, Harbin Engineering University, Harbin 150001, China. [4] State Key Laboratory of Advanced Technology for Materials Synthesis and Processing, Wuhan University of Technology, Wuhan 430070, China. [5] Institut des Sciences Chimiques de Rennes-UMR CNRS 6226, Université de Rennes, Rennes 35042, France.

✉ Corresponding authors. E-mail: S. Lin, linshisheng@fjnu.edu.cn; Y. Xu, xuyinsheng@whut.edu.cn; D. Chen, dqchen@fjnu.edu.cn

Received: December 23, 2025; Revised: February 4, 2026; Accepted: February 8, 2026

fluorides with low phonon energy (< 500 cm^{-1}) into the matrix to increase the scintillation luminescence efficiency. However, due to the internal defects in the disordered structure of glass, the energy cannot be effectively transferred to the luminescent center, leading to low X-ray conversion to visible light efficiency, poor spatial resolution, and poor long-term irradiation.

In this work, a series of Tb^{3+}/Ce^{3+}-codoped Gd-based oxyfluoride LAS glass (LASNT:*x*Gd*y*Ce) was successfully designed and prepared via a melt-quenching method by synergistically introducing Tb_4O_7, GdF_3, and CeF_3. The obtained LASNT:Gd/Ce demonstrated strong green emission with a high internal quantum efficiency (IQE, 97.5%) and outstanding X-ray luminescence properties (XEL, 216% $Bi_4Ge_3O_{12}$ (BGO)), attributed to the synergistic enhancement of energy transfer (ET) efficiency by the combined sensitizers Gd^{3+} and Ce^{3+} to Tb^{3+}. Simultaneously, the developed materials indicated excellent radiation stability under long-term X-ray exposure, achieving a high spatial resolution of up to 32.6 lp·mm^{-1} and a detection limit of 1.03 μGy·s^{-1}, making them suitable for X-ray imaging applications. In addition, the proposed scintillators can be easily processed into flexible shapes and sizes, offering significant possibilities for X-ray imaging.

2 Experimental

2.1 Materials

Preparation of Gd-based oxyfluoride glasses: the glass precursor with the composition of $(51-x)SiO_2$–$25Li_2O$–$5Al_2O_3$–10NaF–$xGdF_3$–$4Tb_4O_7$–$yCeF_3$ (x = 2–7 mol%, y = 0–0.25 mol%) was synthesized via the traditional melt-quenching method. Twenty grams of high-purity raw material was evenly mixed and melted in an alumina crucible at 1450 °C for 90 min. The glass melts were poured into a preheated graphite mold, annealed in a muffle furnace at 500 °C for 2 h to remove internal stress, and cooled to room temperature to obtain the glass precursor. For comparison, the Tb^{3+}-doped oxyfluoride glass was denoted as LASNT, while the Tb^{3+}/Ce^{3+} codoped Gd-based oxyfluoride glass with different contents of GdF_3 and CeF_3 was denoted as LASNT:*x*Gd/*y*Ce. Additionally, the matrix glass and Ce^{3+}-doped Gd-based oxyfluoride glass are labeled LASNT and LASNT:*x*Gd/*y*Ce, respectively (Table S1 in the Electronic Supplementary Material (ESM)). Finally, the prepared glasses were cut and optically polished to a thickness of 2 mm.

2.2 Characterizations

The phase identification of the as-synthesized samples was detected on an X-ray diffractometer (XRD, D8 Advance, Bruker, Germany, Cu Kα light source, λ = 0.154 nm). The absorption and transmission properties of the as-synthesized samples were tested by a ultraviolet–visible (UV–vis) spectrophotometer (Lambda 750S, PerkinElmer, USA). The IQE of LASNT:*x*Gd/*y*Ce was examined by a fluorescence quantum efficiency measurement system (XPOY-EQE-adv, Rhino Spectrum Optoelectronics, China). The XEL, variable temperature XEL spectra, photoluminescence (PL) spectra, and photoluminescence excitation (PLE) spectra of related samples were obtained on a spectrometer (Omni-λ300i, Zolix, China) and fluorescence spectrophotometer (F-7000, Hitachi, Japan), respectively. The X-ray imaging performance of related samples was performed using the self-made X-ray imaging apparatus with a camera sensor size (1-channel complementary metal-oxide-semiconductor (CMOS) 15.86 mm), resolution of 5472 (H) × 3648 (V), and a lens model (MVL-KF3254M-25MP, Hikvision, China). The sample pictures and X-ray imaging photographs were filmed on a mobile phone (under sunlight and 365 nm UV light) and a camera (FL-20BW CMOS, TUSCEN, China), respectively. An X-ray tube (MAGPRO 70 kV 12 W, Moxtek, USA) was employed as the radiation source. X-ray photons were generated at an acceleration voltage of 20 kV and operated within a current range of 50–200 μA. Additionally, the as-synthesized samples for X-ray imaging were polished to 2 mm with a size of 10 mm × 10 mm, and the image acquisition time was 1 s.

3 Results and discussion

3.1 Design and structural characterization of glass

Under X-ray excitation, rare-earth-doped oxyfluoride glass can emit effective luminescence, primarily consisting of three stages: conversion, transmission, and luminescence (Fig. 1). In the conversion stage, the incident X-ray high-energy photons interact with the outer electrons of the atomic nuclei of the glass scintillator to become high-energy free electrons (secondary electrons), primarily through the photoelectric effect. Massive free electrons are ionized to generate low-energy electrons, subsequently from inner-shell orbitals to outer-shell orbitals, forming electron–hole pairs. Subsequently, electron–hole pairs migrate to the luminescent center (rare-earth ions) and release photons through radiative recombination. Evidently, utilizing the sensitization effect of codoped rare-earth ions represents an effective potential pathway for enhancing their scintillation performance.

First, PLE and PL spectra of SiO_2–Li_2O–Al_2O_3–NaF–GdF_3–Tb_4O_7 glass were measured as a function of the GdF_3 content, both of which exhibit typical excitation and emission spectra characteristic of Tb^{3+} (Figs. 2(a) and 2(b)). Compared to the Tb^{3+}-doped sample, the excitation peaks of Gd^{3+} (274 nm, $^8S_{7/2} \rightarrow {}^6I_{7/2}$; 312 nm, $^8S_{7/2} \rightarrow {}^6P_{7/2}$) were observed, confirming an efficient ET process from Gd^{3+} to Tb^{3+} (Fig. S5(a) and Note S1 in the ESM). A series of characteristic emission peaks at 489, 542, 584, and 620 nm was generated under 374 nm excitation, attributed to the $^5D_4 \rightarrow {}^7F_J$ (J = 6, 5, 4, and 3) transitions of Tb^{3+}. In Figs. 2(b) and Fig. S5(a) in the ESM, the luminescence intensity of the LASNT:*x*Gd samples first increased and then decreased as the GdF_3 content increased, exhibiting optimal PL properties at x = 4 mol%, which may be attributed to excessive Gd^{3+} consuming energy through charge migration or nonradiative transitions (e.g., $^6P \rightarrow {}^8S$ transition of Gd^{3+}). Figure 2(c) shows the IQE spectra of LASNT:*x*Gd as a function of GdF_3 doping concentration. The IQE achieved a maximum value of 96.8% at x = 4 mol% (Fig. S1(a) and Note S2 in the ESM). From the perspective of the glass network structure, the initial glass network structure primarily consists of [SiO_4] and [AlO_4] tetrahedra units (Figs. 2(d) and S1(b) in the ESM). When small amounts of GdF_3 were incorporated, the glass network structure partially depolymerized to form [SiO/F_4] and [AlO/F_4] units. Given that the vibrational frequency of the Tb–F bond (350 cm^{-1}) is lower than that of the Tb–O bond (600–900 cm^{-1}), the phonon energy in the glass matrix is significantly reduced, leading to substantial suppression of multiphoton relaxation processes and thus enhancing the luminescence efficiency of the material. Moreover, when the concentration of GdF_3 increased from 2 to 4 mol%, the energy gap between the $^5D_4 \rightarrow {}^7F_J$ (J = 6, 5, 4, and 3) level of Tb^{3+} narrowed due to lattice expansion, resulting in enhanced ET efficiency (Fig. 2(e)). However, a significant depolymerization of the glass network occurred at excessive GdF_3 concentrations (accompanied by Gd^{3+} aggregation/cross-relaxation and locally high-phonon density),

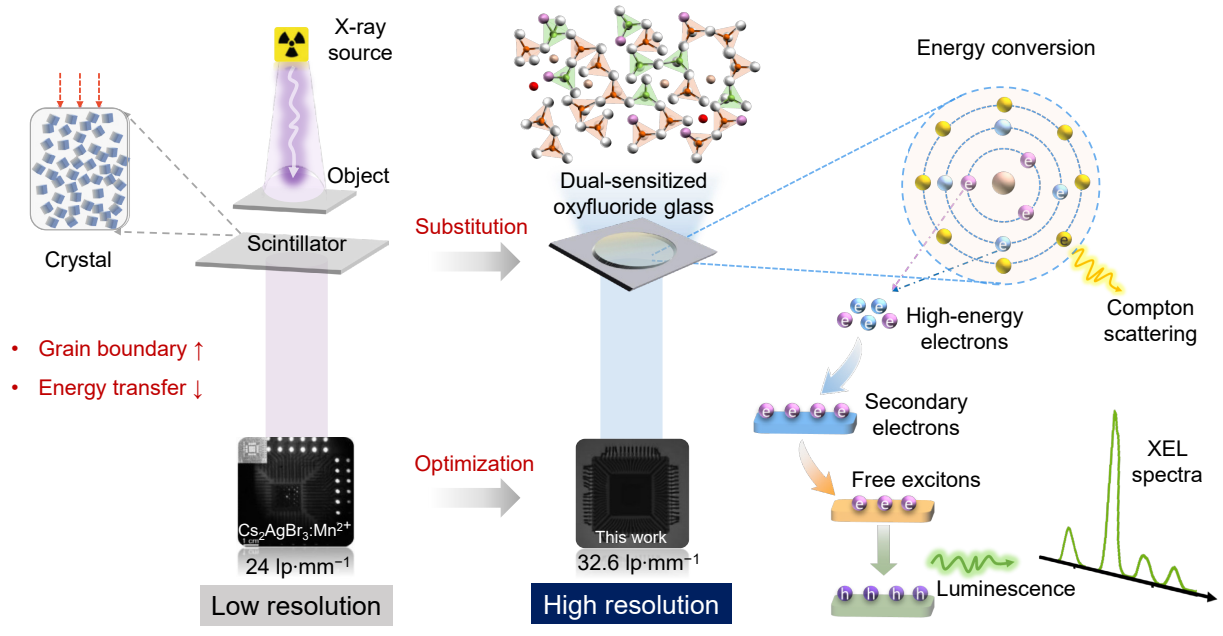

Fig. 1 Schematic design of an alternative high-transparency oxyfluoride glass scintillator-based X-ray imaging system. By employing a dual sensitization strategy within oxyfluoride glass matrix, ET is optimized, and grain boundary effects are minimized. Compared to $Cs_2AgBr_3:Mn^{2+}$ crystal, the designed scintillator achieves a high resolution of 32.6 lp·mm^{-1}.

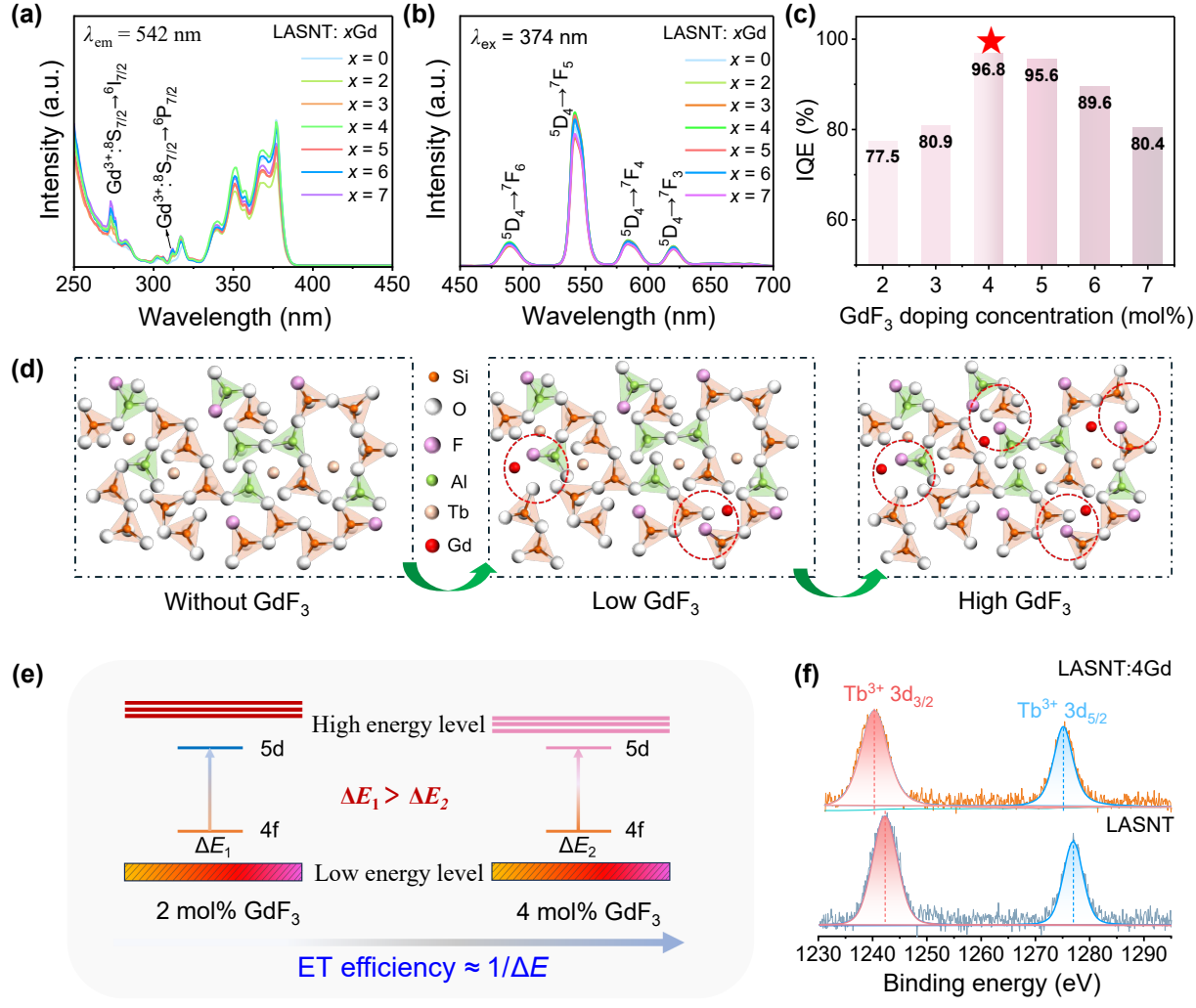

Fig. 2 (a) PLE (λ_{em} = 542 nm) and (b) PL spectra (λ_{ex} = 374 nm) of LASNT:*x*Gd samples. (c) IQE spectra of LASNT:*x*Gd as a function of GdF_3 doping concentration. (d) Schematic diagram of changes in the glass network structure before and after the introduction of GdF_3. (e) Schematic representation of charge transfer quenching of Tb^{3+} ions in glass. (f) XPS spectra of Tb 3d.

清華大学出版社 Tsinghua University Press | SciOpen

leading to a decrease in luminescence intensity, which may be attributed to defect-induced nonradiative transitions [28]. In Fig. 2(f), the XPS Tb 3d spectra show that the peak shifts toward higher binding energies, further indicating that excited Gd^{3+} efficiently transfers energy nonradiative to Tb^{3+}, accompanied by an enhancement in the ionic hybrid nature of the Tb–F bond.

3.2 ET and optical properties

Furthermore, the introduction of CeF_3 as a cosensitizer enhanced the luminescence properties of LASNT:4Gd, and all LASNT: 4Gd*y*Ce samples exhibited totally amorphous phases (Fig. S2(a) in the ESM). Simultaneously, the introduction of CeF_3 has no significant effect on the intrinsic robustness of the glass network structure, thereby facilitating its high light output and irradiation stability (Fig. S2(c) in the ESM). The excitation band of Tb^{3+} at 330–390 nm and the emission of Ce^{3+} at 360–500 nm overlap, which indicates the existence of ET from Ce^{3+} to Tb^{3+} (Fig. S3(a) in the ESM). PLE spectra (λ_{em} = 542 nm) of LASNT:4Gd*y*Ce (y = 0.05–0.2 mol%) samples were studied and are shown in Fig. 3(a), and the broad excitation band was attributed to the $4f^1 \rightarrow 5d^1$ transition of Ce^{3+} ions, suggesting the presence of ET from $Ce^{3+} \rightarrow Tb^{3+}$ in these samples (Note S1 in the ESM). Upon irradiation at 374 nm, the main emission peaks of the LASNT:4Gd*y*Ce sample at 489, 542, 583, and 621 nm exactly match $^5D_4 \rightarrow {}^7F_6$, $^7F_5$, $^7F_4$, and $^7F_3$ of Tb^{3+} (Fig. 3(b)). Notably, the broad excitation band observed at 321 nm is attributed to the 4f–5d transition of Ce^{3+}, with the corresponding emission band occurring at 365 nm (Fig. S4(a) in the ESM). As such, PL measurements conducted on the LASNT: 4Gd*y*Ce scintillator under 374 nm excitation revealed only emission from Tb^{3+} ions. The typical PL time decay curve of the Tb^{3+} 4f–4f transition follows a single-exponential function of 2.59 ms. As the concentration of Ce^{3+} increased, the lifetime of the LASNT:4Gd*y*Ce glass initially rose from 2.59 to 2.64 ms and subsequently decreased to 2.57 ms, which exhibits a characteristic double-exponential decay (Note S2 in the ESM). The observed decline can be attributed to a valence state transition within the Ce^{3+}-containing glass, which reduces the probability of direct hole-electron recombination, thus diminishing the ET from Ce^{3+} to Tb^{3+} (Fig. 3(d)) [29].

Due to the ET process above, compared to LASNT:4Gd, the PL intensity of LASNT:4Gd*y*Ce (y = 0.05–0.2 mol%) was significantly enhanced, with the optimal PL sample being LASNT:4Gd0.05Ce. As the CeF_3 content increases, the PL intensities of the LASNT:4GdyCe samples first increase and then decrease, indicating that Ce^{3+} ions sensitize and enhance the luminescence

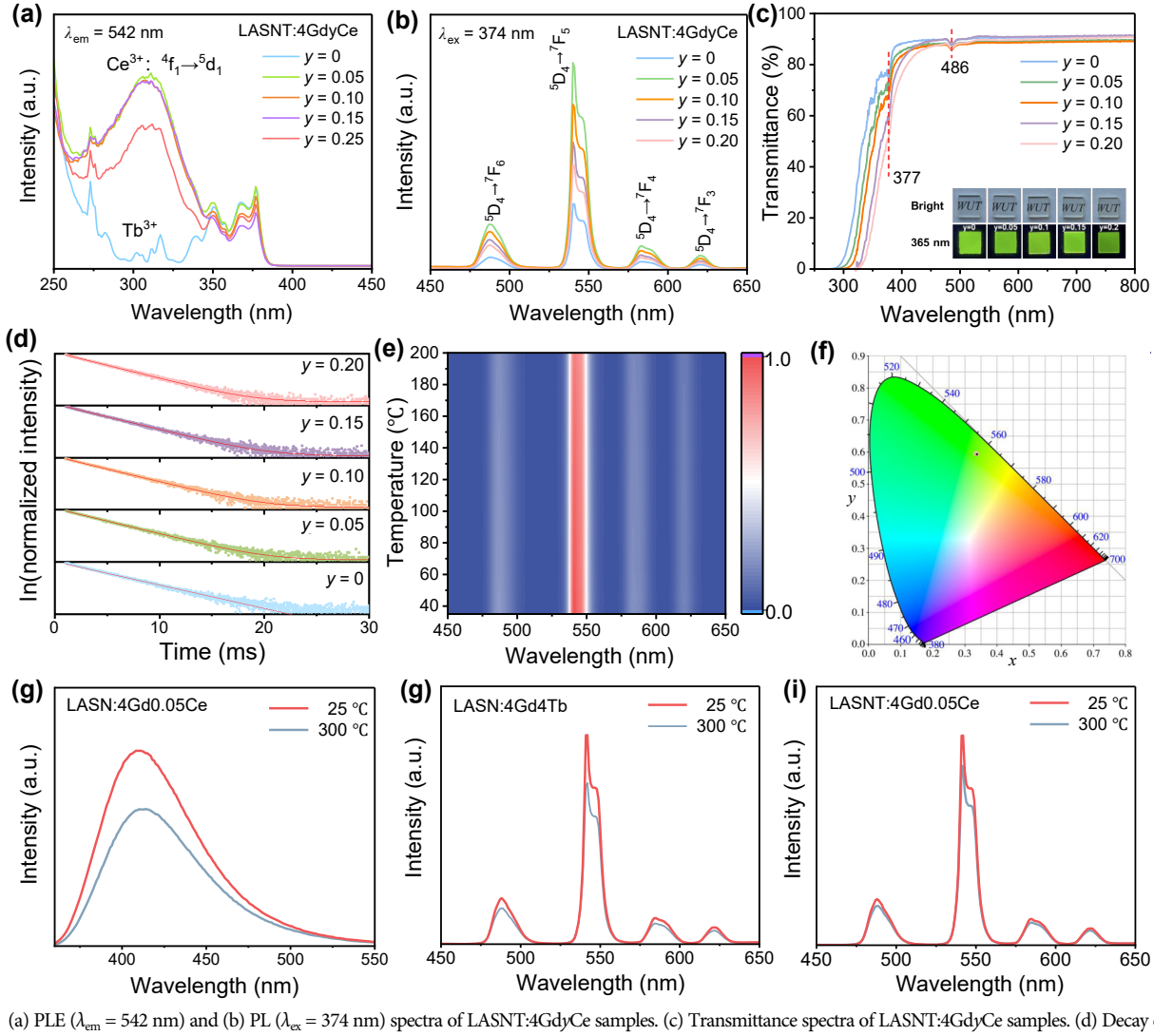

Fig. 3 (a) PLE (λ_{em} = 542 nm) and (b) PL (λ_{ex} = 374 nm) spectra of LASNT:4Gd*y*Ce samples. (c) Transmittance spectra of LASNT:4Gd*y*Ce samples. (d) Decay curves (λ_{ex} = 374 nm) of LASNT:4Gd*y*Ce samples. (e) 2D contour plot of temperature-dependent PL spectra for LASNT:4Gd0.05Ce. (f) CIE chromaticity diagram of LASNT:4Gd*y*Ce glasses, integrated PL intensities of (g) LASNT:4Gd0.05Ce, (h) LASNT:4Gd, and (i) LASN:4Gd0.05Ce at 25 and 300 °C, respectively.

performance of LASNT:4Gd (Figs. 3(b) and S5(d) in the ESM). In Fig. S4(b) in the ESM, the obtained sample achieved a high IQE and EQE of 97.5% and 84.4%, respectively. Due to the ET from the 5d–4f of the Ce^{3+} electron transition to Tb^{3+}, the luminescence intensity of the sample was enhanced, while simultaneously causing its absorption peak to gradually broaden (Fig. S2(b) in the ESM). Correspondingly, compared to LASNT:4Gd, the refractive index of LASNT:4Gd0.05Ce increases by approximately 0.02–0.04 in the long-wavelength region, indicating enhanced local polarizability that favors increased radiation transition probability (Fig. S3(b) in the ESM). Furthermore, high optical transmittance is essential for ensuring the imaging properties of glass scintillators, and LASNT:4Gd*y*Ce exhibited a transmittance of approximately 90% in the visible light region, making it suitable for X-ray imaging applications (Fig. 3(c)).

On the other hand, the optimized LASNT:4Gd0.05Ce demonstrated exceptional PL thermal stability, with the overall PL intensity at 300 °C remaining at 86.3% of its initial intensity at 25 °C (Figs. 3(e) and 3(i)). Meanwhile, the PL intensities of LASNT:4Gd and LASNT:4Gd0.05Ce were diminished to 77.4% and 68.6% of their initial values at 25 °C, respectively (Figs. 3(g) and 3(h)). These results demonstrate that thermally enhanced electron transfer effectively compensates for thermal quenching effects, thus achieving superior luminescence performance and thermal stability. Additionally, Fig. 3(f) shows the CIE standard diagram and the calculated chromaticity of LASNT:4Gd*y*Ce, with all samples exhibiting bright green light emission (Table S3 in the ESM).

3.3 XEL properties and X-ray imaging application

To further investigate their scintillation properties, the X-ray absorption efficiency of the prepared glass samples was evaluated over a photon energy range of 10^0–10^3 keV, with the LASNT:4Gd0.05Ce exhibiting outstanding X-ray absorption, slightly lower than that of the same-sized (15 mm × 15 mm × 2 mm) commercial BGO (Fig. 4(a) and Table S2 in the ESM); however, the integrated RL spectra of LASNT:4Gd*y*Ce are 209%, 216%, 212%, 210%, and 201% of that BGO, respectively (Figs. 4(b)

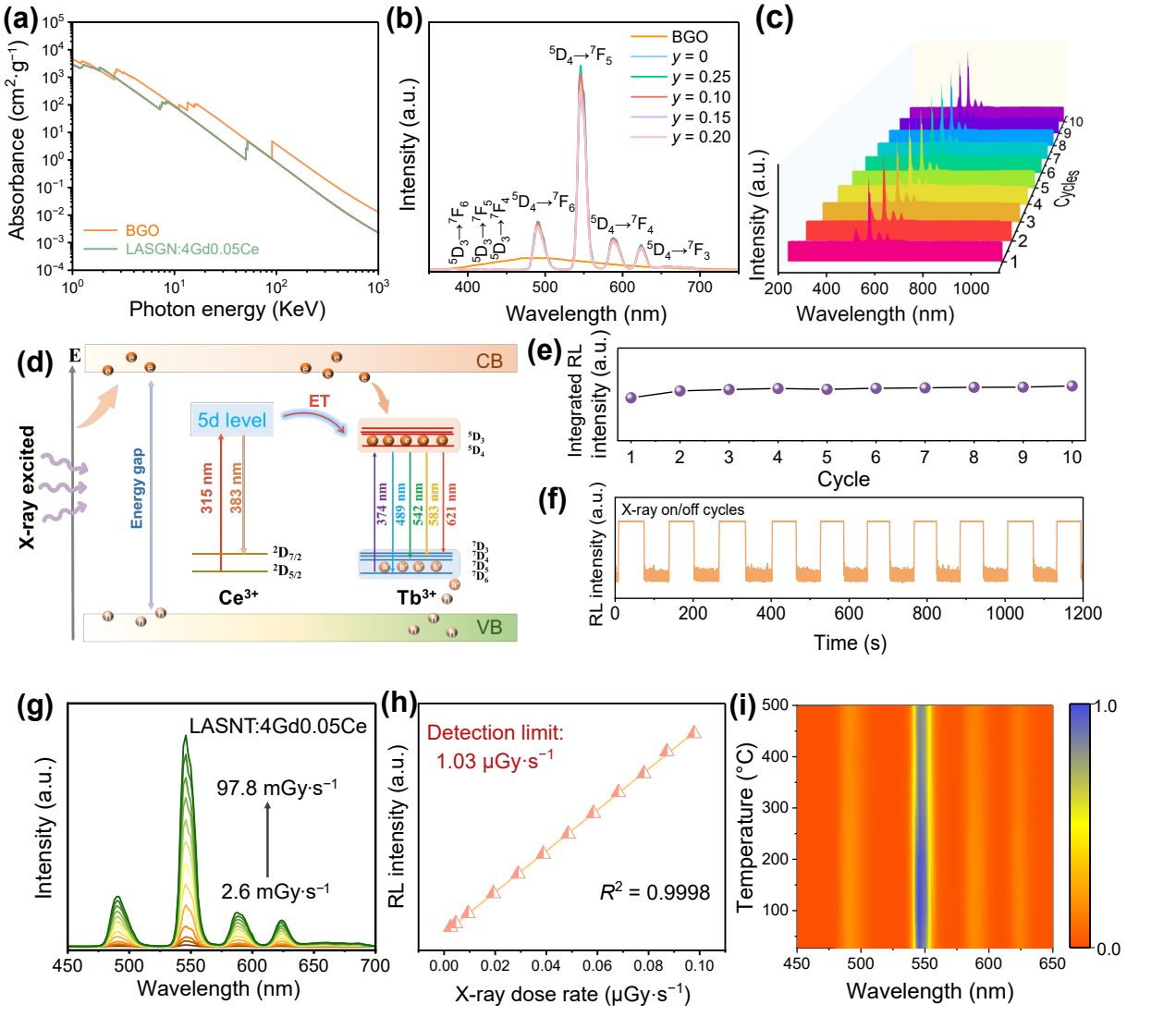

Fig. 4 (a) Calculated X-ray absorption coefficients of commercial BGO and LASNT:4Gd0.05Ce as a function of photon energy. (b) XEL spectra of LASNT:4GdyCe compared with an equivalently shaped BGO. (c) XEL spectra of LASNT:4Gd0.05Ce under repeated 10 X-ray irradiation cycles. (d) Schematic illustration of RL mechanism of LASNT:4Gd0.05Ce specimen. (e) Integrated XEL intensity varies spectra of LASNT:4Gd0.05Ce with the number of operations. (f) Time-dependent RL intensity of LASNT:4Gd0.05Ce under continuous turn-on/off X-ray irradiation at 50 kV and 220 mA. (g) XEL spectra measured under various X-ray dose rate irradiation ranging from 2.6 to 97.8 mGy·s^{-1}. (h) RL intensity as a function of X-ray dose rate for LASNT:4Gd0.05Ce. (i) 2D contour plot of temperature-dependent RL spectra for LASNT:4Gd0.05Ce.

清華大学出版社 Tsinghua University Press | SciOpen

and S6(a) in the ESM), indicating that while the developed material has slightly lower X-ray absorption efficiency, its efficiency in converting X-ray to visible light is significantly higher. Meanwhile, the integrated RL intensity of LASNT:4Gd0.05Ce was approximately 1.06 times higher than that of LASNT:4Gd. It is evident that Tb^{3+} serves as the luminescent center because the introduction of Ce^{3+} and Gd^{3+} ions can significantly enhance the scintillation properties. Specifically, upon incorporation of CeF_3 into the glass matrix, Ce^{3+} ions absorb high-energy X-ray energy and then efficiently transfer it to the luminescent center of Tb^{3+} via nonradiative leaps, prompting LASNT:4Gd0.05Ce to emit characteristic green fluorescence during the 4f–4f transition ($^5D_4 \rightarrow {}^7F_5$), thus achieving energy-enhanced coupling (Fig. 4(d)) [29].

In addition, X-ray irradiation stability is one of the key indicators for the practical application of glass scintillators. As demonstrated in Figs. 4(c) and 4(e), the RL intensity and integrated RL intensity as a function of irradiation cycles were tested, revealing that the RL intensity remained consistently stable throughout sustained X-ray exposure, with no significant quenching effect observed. After 1200 s of X-ray on/off cycles, the relative RL intensity of the LASNT:4Gd0.05Ce sample remained essentially stable, indicating its excellent X-ray switching response capability and irradiation stability (Fig. 4(f)). Figure S6(b) in the ESM shows the XEL intensity of the LASNT:4Gd0.05Ce sample at various irradiation powers (0.1–10 W), which gradually rose as the X-ray power increased and remained virtually undamaged even under high-dose radiation. The detection limit of LASNT:4Gd0.05Ce was further obtained by the measurement of photocurrent at different X-ray dose rates (2.6–97.8 $mGy \cdot s^{-1}$), and the lowest detection limit was 1.03 $\mu Gy \cdot s^{-1}$ based on linear fitting with a signal-to-noise ratio (SNR) of 3 (Figs. 4(g) and 4(h)), which is lower than the dose rate required for X-ray medical diagnosis (5.5 $\mu Gy \cdot s^{-1}$) [30,31]. Specifically, the low detection limit is obtained by fitting the RL intensity, mainly due to Tb doping induction, but is not equivalent to low-dose-rate X-ray imaging. In addition, the variable-temperature RL spectra were measured, revealing that the sample also exhibits excellent RL resistance to thermal quenching (Figs. 4(i) and S7 in the ESM).

Furthermore, based on an X-ray imaging system (composed of an X-ray source, a scintillator, an optical reflector, and a camera), the application potential of the developed glass scintillator for high-resolution imaging was constructed (Fig. 5(a)). The internal structure of all images (spring-loaded capsules and chips) is clearly visible with well-defined boundaries, achieving an observed resolution of ~30 $lp \cdot mm^{-1}$ (Figs. 5(c) and 5(d)). Meanwhile, the modulated transfer function (MTF) of LASNT:4Gd0.05Ce (thickness: 2 mm) was further measured using the slanted edge method, showing a high spatial resolution of 32.6 $lp \cdot mm^{-1}$, which surpasses the performance of most existing reported glass scintillator materials. (Figs. 5(d) and 5(f); Note S2 and Table S4 in the ESM). After continuous X-ray imaging testing (approximately 6 h), the IQE of the LASNT:4Gd0.05Ce sample decreased by only 1.9%, exhibiting excellent irradiation stability (Fig. 5(e)). In addition, the developed glass scintillator can be successfully manufactured in irregular shapes (e.g., stars and heart shapes) and at a large scale (diameter: 5 cm) (Figs. 5(a) and 5(b)), indicating its significant application potential for X-ray imaging.

4 Conclusions

In summary, a high-performance Ce and Tb codoped Gd-based glass scintillator material has been successfully developed.

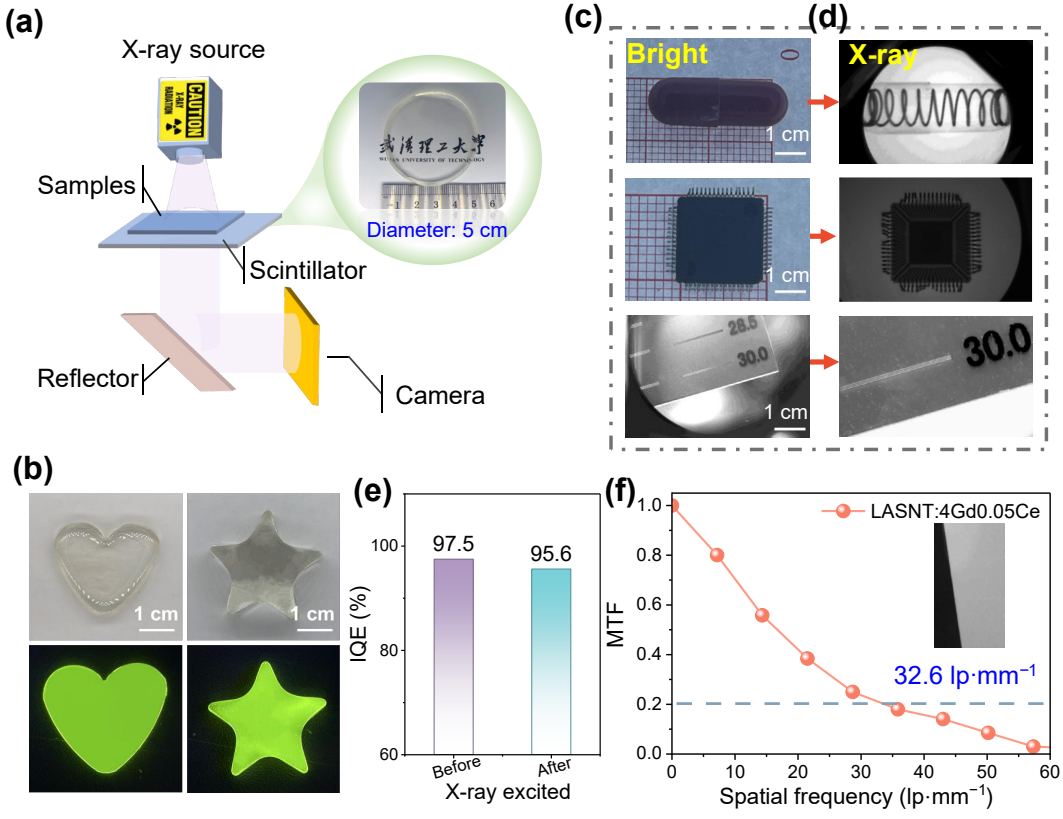

Fig. 5 (a) Schematic diagram of designed indirect X-ray imaging system. (b) Photograph of complex-shaped LASNT:4Gd0.05Ce sample under daylight and 365 nm excitation. (c) Sample imaging and (d) X-ray imaging of springs, chips, and standard line-pair card. (e) IQE of LASNT:4Gd0.05Ce sample before and after continuous X-ray imaging measurements (approximately 6 h). (f) MTF curve of sample obtained using slanted edge method.

Through systematic optimization of doping concentrations, we determined the optimal codoped Gd^{3+} and Ce^{3+} concentrations (4 and 0.05 mol%) for achieving maximum RL intensity. Its scintillation intensity was significantly enhanced compared to that of the unmodified material (LASNT scintillator), with a high IQE reaching 97.5% and a high XEL intensity (216%BGO). Meanwhile, the LASNT:4Gd0.05Ce scintillator exhibits high optical transmittance (~90% at 550 nm), low detection limits (1.03 $\mu Gy \cdot s^{-1}$), and excellent irradiation stability. The X-ray imaging based on the developed glass scintillator achieved a high resolution of 32.6 $lp \cdot mm^{-1}$, surpassing previously most reported scintillator materials. Evidently, the developed material demonstrates significant application potential in high-resolution X-ray imaging.

Acknowledgements

This work is financially supported by the National Natural Science Foundation of China (Nos. U2241236, U2330115, and 62275206) and the Key Research & Development Project of Hubei Province (No. 2022BAA025).

Availability of data and materials

Data will be made available on request.

Competing interests

The authors have no competing interests to declare that are relevant to the content of this article. The author Daqin Chen is the Editorial Committee member of this journal.

Electronic Supplementary Material

Supplementary material is available in the online version of this article at https://doi.org/10.26599/JAC.2026.9221259.

References

[1] Chen QS, Wu J, Ou XY, *et al.* All-inorganic perovskite nanocrystal scintillators. *Nature* 2018, **561**: 88–93.
[2] Chen WQ, Zhou M, Liu Y, *et al.* All-inorganic perovskite polymer–ceramics for flexible and refreshable X-ray imaging. *Adv Funct Mater* 2022, **32**: 2107424.
[3] Wang JX, Shekhah O, Bakr OM, *et al.* Energy transfer-based X-ray imaging scintillators. *Chem* 2025, **11**: 102273.
[4] Brechtl J, Xie X, Feng R, *et al.* Serrated flow in NaI:Tl scintillator crystals. *J Mater Sci Technol* 2023, **153**: 120–127.
[5] Zhou FG, Li ZZ, Lan W, *et al.* Halide perovskite, a potential scintillator for X-ray detection. *Small* 2020, **4**: 2000506.
[6] Sui ZX, Qian S, Niu LY, *et al.* Glass scintillator: A window to future high-energy radiation detection. *Innovation* 2025, **6**: 100878.
[7] Zhang H, Yang Z, Zhou M, *et al.* Reproducible X-ray imaging with a perovskite nanocrystal scintillator embedded in a transparent amorphous network structure. *Adv Mater* 2021, **33**: 2102529.
[8] Ma WB, Jiang TM, Yang Z, *et al.* Highly resolved and robust dynamic X-ray imaging using perovskite glass-ceramic scintillator with reduced light scattering. *Adv Sci* 2021, **8**: 2003728.
[9] Liu JQ, Zhao XD, Xu YS, *et al.* All-inorganic glass scintillators: Scintillation mechanism, materials, and applications. *Laser Photonics Rev* 2023, **17**: 2300006.
[10] Zhao JT, Fan ZH, Zhou S, *et al.* Defect assisted multicolor luminescence in borosilicate photonic glass for high-level anticounterfeiting and X-ray imaging. *Adv Funct Mater* 2025, **35**: 2503714.
[11] Zhao CH, Wang YZ, Bao SY, *et al.* High-performance hybrid organic-inorganic lanthanide halide glass scintillators enabled by dehydration for efficient X-ray imaging. *Adv Mater* 2025, **37**: 2500925.
[12] Zhang S, Yang XX, Xiao JQ, *et al.* Tunable full-color mechanoluminescence in rare earth-doped transparent amorphous glass. *Adv Funct Mater* 2024, **34**: 2404439.
[13] Yang D, Ge K, Ban HY, *et al.* High transparency Ce^{3+}-doped oxyfluoride glass scintillator for X-ray imaging and γ-ray detection. *Ceram Int* 2024, **50**: 47253–47258.
[14] Luo CX, Jing Y, Hua ZH, *et al.* Band gap and defect engineering enhanced scintillation from Ce^{3+}-doped nanoglass containing mixed-type fluoride nanocrystals. *ACS Appl Mater Inter* 2023, **15**: 46226–46235.
[15] Wantana N, Kaewnuam E, Chanthima N, *et al.* Ce^{3+} doped glass for radiation detection material. *Ceram Int* 2018, **44**: 172–176.
[16] Kuang YH, Jin JC, Liu GC, *et al.* $KBaScSi_3O_9:Eu^{2+}$ glass-ceramics as single-phase high-power white emitters. *Adv Funct Mater* 2025, **35**: 2418751.
[17] Li XY, Yang CB, Qiu LT, *et al.* $NaAlSiO_4:Eu^{2+}$ glass ceramics: Self-reduced *in situ* growth and high-power LED/LD lighting. *Laser Photonics Rev* 2022, **16**: 2100346.
[18] Li LJ, Zou JH, Chen JY, *et al.* Eu^{2+} doped glass scintillators with high-scintillating performances for X-ray imaging. *Mater Today Chem* 2025, **46**: 102724.
[19] Li XY, Shen ZY, Zhu YW, *et al.* Single band of red upconverison emission in Ce-based glass ceramics for light manipulation. *J Lumin* 2020, **227**: 117527.
[20] Song MJ, Wang LT, Wang J, *et al.* Constructing double perovskite Eu^{3+}/Mn^{4+}-codoped $La_2Mg_{1.33}Ta_{0.67}O_6$ phosphors for high sensitive dual-mode optical thermometers. *J Lumin* 2022, **252**: 119347.
[21] Li LJ, Chen JY, Wen ZX, *et al.* X-ray imaging scintillator: Tb^{3+}-doped oxyfluoride aluminosilicate glass. *Ceram Int* 2024, **50**: 757–763.
[22] Zhang DD, Lin SS, Xia ML, *et al.* Flexibly prepared Tb^{3+}-doped oxyfluoride glass scintillators with enhanced luminescence for X-ray imaging and detection. *Laser Photonics Rev* 2025, **19**: 2500354.
[23] Wang L, Lu FM, Wei RF, *et al.* Superior scintillation property of Tb^{3+}-doped sodium silicate glass. *Ceram Int* 2022, **48**: 21945–21950.
[24] Pang T, Lin SS, You FL, *et al.* Synergistic enhancement of crystallinity and transparency in Tb^{3+}-doped nano-glass-ceramics for high-resolution X-ray imaging. *J Adv Ceram* 2025, **14**: 9221122.
[25] Venkateswaran C, Sreemoolanadhan H, Vaish R. Lithium aluminosilicate (LAS) glass-ceramics: A review of recent progress. *Int Mater Rev* 2022, **67**: 620–657.
[26] Zheng JY, Liu JW, Liang YR, *et al.* Advancing high-power laser lighting: Designing a novel YAGG:Ce color converter in Li–Al–Si glass ceramic. *Laser Photonics Rev* 2024, **18**: 2400563.
[27] Zheng T, Li MH, Ma YP, *et al.* Kinetic analysis of the crystallization of Y_2O_3 and La_2O_3 doped $Li_2O–Al_2O_3–SiO_2$ glass. *RSC Adv* 2024, **14**: 7052–7060.
[28] Li C, Zhang X, Onah VC, *et al.* Physical and optical properties of $TeO_2–WO_3–GdF_3$ tellurite glass system. *Ceram Int* 2022, **48**: 12497–12505.
[29] Zu CK, Chen J, Zhao HF, *et al.* Effect of cerium on luminescence and irradiation resistance of Tb^{3+} doped silicate glasses. *J Alloys Compd* 2009, **479**: 294–298.
[30] Pan L, Shrestha S, Taylor N, *et al.* Determination of X-ray detection limit and applications in perovskite X-ray detectors. *Nat Commun* 2021, **12**: 5258.
[31] Long GL, Winefordner JD. Limit of detection a closer look at the IUPAC definition. *Anal Chem* 1983, **55**: 712–724.